Characterization of the bubble cluster and velocity field in the focal region of a lithotripter

2007 New J. Phys. 9 240

(http://iopscience.iop.org/1367-2630/9/7/240)

New Journal of Physics
The open–access journal for physics

Characterization of the bubble cluster and velocity field in the focal region of a lithotripter

J M Buick[1], J A Cosgrove[2,3], H Eizenhöfer[4], R Higham[2] and R Royles[5]

[1] Physics and Electronics, University of New England, NSW 2351, Australia
[2] Fluids and Acoustics Group, School of Physics, The University of Edinburgh, Kings Buildings, Edinburgh EH9 3JZ, UK
[3] Professional Scientific Limited, ETTC Biospace, Kings Buildings, Edinburgh EH9 3JF, UK
[4] Dornier MedTech Systems GmbH, Argelsrieder Feld 7, D-82234 Wessling, Germany
[5] Institute for Infrastructure and Environment, School of Engineering and Electronics, The University of Edinburgh, Kings Buildings, Edinburgh EH9 3JN, UK
E-mail: jbuick@une.edu.au

New Journal of Physics **9** (2007) 240
Received 28 February 2007
Published 20 July 2007
Online at http://www.njp.org/
doi:10.1088/1367-2630/9/7/240

Abstract. The cavitation bubble cluster and the velocity field in the focal region of a lithotripter are investigated. Images of the bubble cluster were captured which show the bubbles increasing in size over approximately 500 μs before collapsing rapidly. Velocity measurements were obtained using particle image velocimetry. A few milliseconds after the inception of cavitation the velocity field consisted of localized flows with maximum velocities and shear rates of the order of 100 mm s^{-1} and 50 s^{-1} respectively. At times 40 ms after cavitation an average uni-directional flow of the order of 10 mm s^{-1} was observed. The mechanism by which the flow is generated is also considered.

PII: S1367-2630(07)44930-8

Contents

1. Introduction

The use of shock wave lithotripters has proved highly effective when applied to destroying kidney stones [1]. The lithotripter head produces a pressure pulse which is focused in the region of the stone being treated, where the magnitude of the pressure pulse is magnified by more than two-orders of magnitude and the front steepens into a shock wave. The technique is now applied in hospitals world wide and has been used to successfully treat many hundreds of thousands of patients. Cavitation [2] is observed in the focal region of a lithotripter and is thought to play a role not only in kidney stone fragmentation [3], but also in causing damage to the kidney [4, 5]. Various aspects of cavitation related to lithotripsy have been investigated [6, 7] as well as jet formation from a collapsing bubble [8]. A number of studies have considered the bubble clusters [9]–[12]; however, velocity fields, which have been observed in the region of the cavitation, have not been studied to the same extent. It is possible that these flows and their associated shears also contribute to tissue damage [13, 14]. The mechanism by which they are generated is unclear. In a recent study [12], concerned primarily with the dynamics of bubble clusters, fluid velocities were also measured. In a region close to the focus of the lithotripter the maximum fluid velocity increased to a maximum around 200 ms after the lithotripter was triggered. The maximum velocity was then decayed to the background level in the subsequent 1 s. The mechanism responsible for generating the flow was not considered.

This investigation is concerned with the characterization of the bubble cluster which forms due to cavitation and the velocity field, both in the focal region of a lithotripter. For this work particle image velocimetry (PIV), which is a powerful wholefield fluid velocity measurement technique, was chosen. Conceptually PIV can be understood in a straightforward manner. A number of seeding particles are added to the fluid which are sufficiently small to follow the flow [15]. A pair of images of the seeding particles are taken with a known time separation and the displacement of the particles between the images is found. From this it is straightforward to calculate the velocity of the seeding particles and hence of the flow. In practice each step incorporates a number of procedures each of which requires careful consideration and implementation. Full details of the technique can be found elsewhere, see for example [16]–[18]. The same system, without the velocity analysis, can be applied to study the bubble cluster.

In this paper, the bubble cluster and velocity field generated in the focal region of the lithotripter are considered along with the mechanism by which the flow is generated. This has direct applications to the field of lithotripsy providing an improved understanding of the processes involved. In addition, the potential of the flow and associated shear to produce tissue damage can be assessed. Details of the mechanism by which the flow is generated are also of more general interest as an example of a system where acoustic fields and fluid motion interact. There are a number of mechanisms which are considered as potential flow generators. One possibility is the rapid collapse of the bubbles. This produces a pressure variation in the fluid and an associated velocity field. It is well known that asymmetric bubble collapse produces a high velocity jet [8, 19], for example when a bubble collapses near a solid wall, such as a ship propeller, structural damage can occur. Jets are observed also during the collapse of a spherical bubble when the symmetry is broken either by the growth of small perturbations or by a nearby surface. An alternative possible mechanism is acoustic streaming which is a mean flow known to be generated in high intensity acoustic fields [20]–[22]. In these flows one expects fluid particles to oscillate back and forth about a mean position, transmitting energy but with no mean bulk fluid motion. It is therefore perhaps initially surprising when one observes a net fluid motion. Thus there are two different flow velocity regimes associated with sound. The first is the oscillatory component associated with a propagating wave and the second is the more subtle, second-order, time-averaged flow associated with high intensity sound. A detailed description can be found in, for example [20, 22, 23].

2. Experimental arrangement and procedure

The experimental rig comprised a perspex tank (450 mm long $\times$300 mm wide $\times$300 mm deep) filled with tap water to a depth of 260 mm. The water was left overnight to remove any excess air from the filling process. Other than this the water was not degassed. The measurements were taken at a water temperature of 20 °C. The head of the electromagnetic lithotripter[6] was incorporated into the tank through a circular section cut from one of the sides as shown in figure 1. A plane pressure pulse propagating from a thin membrane in the lithotripter head was focused by an acoustic lens and was generated by a high voltage discharge from a capacitor into an inductance coil arrangement. A charging and triggering unit served as a driver for the capacitor arrangement with a dc voltage signal in the range (0–4 V) from a variable power supply controlling the level of charge (0–16 kV) for the driver and hence the capacitor. Since the intensity of the pressure wave was dependent on the charge of a capacitor, this provided a simple and flexible method to adjust the pressure levels of the shockwave. A polyurethane rubber absorber[7] was placed at the opposite end of the tank to the lithotripter head.

The measurement zone comprised an area several hundred square millimetres around the focal region of the pressure wave as shown in figure 1. This region was illuminated using a 20 W pulsed copper vapour laser (LS20-50)[8] which produced two wavelengths of light $\lambda = 510.6$ and $\lambda = 578.2$ nm with a pulse duration of 30 ns. The light from the laser was directed to the test area using a fibre optic cable. An optical arrangement attached to the end of the fibre optic cable converted the laser beam into a laser sheet. This light sheet illuminated tracer nylon

[6] Supplied by Dornier MedTech, Germany.
[7] Acoustic absorber type F28: National Physics Laboratory, Teddington, UK.
[8] Oxford lasers Ltd, Abingdon, Oxon OX14 3YR, UK.

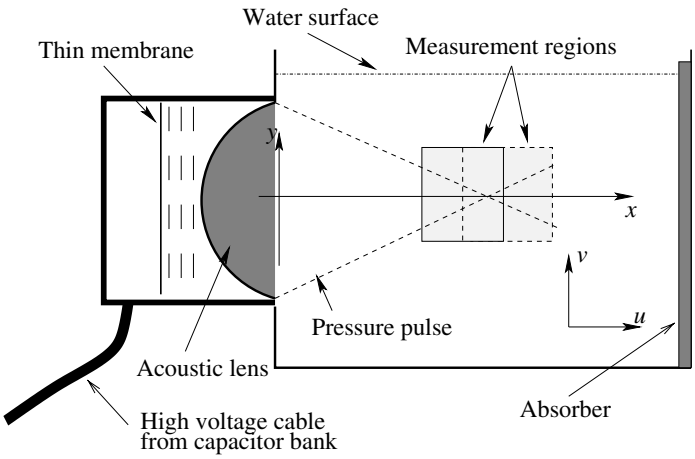

Figure 1. Schematic of lithotripter and tank arrangement.

microspheres which had been added to the water in the tank. These particles had a relative density of 1.03 and a mean particle diameter of $20 \pm 4\,\mu$m and followed the flow very accurately, see appendix. The total mass of nylon particles was 3 g giving a particle density of approximately 20 particles mm^{-3}. The side scattered light from the tracer particles was focused on to the CCD (charged coupled device) element of a PCO camera[9] using a 55 mm Micro-Nikkon lens (with $f^{\#} = 2.8$).

The timings of the laser, PCO camera and lithotripter were controlled by a pair of Berkeley timing boxes. A signal, manually triggered from one of these boxes, was fed into a pulse generator which produced the relevant signal to trigger the capacitor bank. A small induction loop placed on the high voltage cable (between the capacitor bank and membrane as shown in figure 1, was used to monitor the membrane activation. A Brüel and Kjær 8103 hydrophone placed in the tank monitored the temporal propagation of the pressure wave. The relative timings between the membrane triggering and the pulse propagation were as expected ($c \simeq 1.5\,\text{mm}\,\mu\text{s}^{-1}$ where c is the speed of sound in water). Between sets of velocity measurements, the hydrophone was replaced in the tank and pressure waves were generated to ensure the timings were consistent.

The PCO camera was used in double image capture mode which enabled two separate images to be recorded with a variable separation time. The images were analysed using a cross correlation algorithm which was implemented using fast Fourier transforms, as shown in figure 2 with an interrogation region of 32×32 pixels and a 16×16 grid spacing. The scale of the images was 1280 pixels to 53 mm giving a vector spacing of 0.66 mm. The time separation between images (Δt) was adjusted to suit the event being captured. For figures 5–7 separations of up to 1 ms were used. For figures 8 and 9 separations of up to 3 ms were used. A local median filter was used to validate and interpolate spurious vectors caused by random effects such as the intermittent lack of seeding in areas of an image.

To ensure that the images recorded had a sufficient resolution two separate measurement regions were considered. The measurement regions consisted of an area mainly before or after the focal point of the acoustic lens with the measurement region including the acoustic focus in each case. This is shown schematically in figure 1. Precise details of the location of the image are shown on the axes of the relevant results.

[9] SensiCam (double shutter) 12 bit cooled S/N 370 KD 1983.

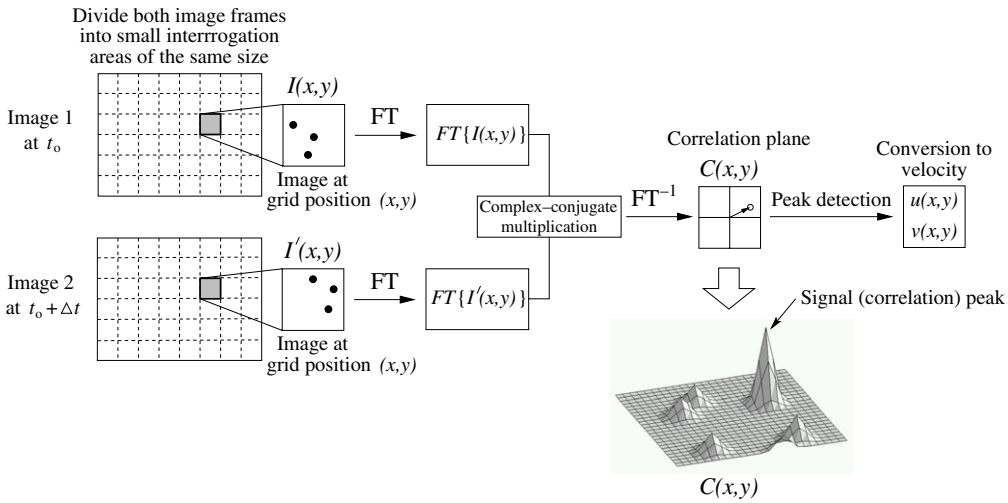

Figure 2. Cross correlation algorithm.

The growth rates of cavitation bubbles were observed by capturing two consecutive images on the PCO camera separated by relatively small time intervals. These time intervals were monitored and controlled using the Berkeley timing boxes and a digital storage oscilloscope. To characterize the velocity field and in particular investigate its generation mechanism, a large number of image pairs were recorded at various time intervals before and after cavitation (within the cavitation region itself the reflections and refractions caused by the numerous bubbles rendered the velocity information redundant). Again the time intervals were monitored and controlled using the timing apparatus. Between the acquisition of each image pair the fluid in the tank was allowed to settle to ensure that the captured motion was generated from the lithotripter pulse. The remnants of previous motion prior to capturing a new set of data were less than 1 mm s^{-1}.

3. Results and discussion

The pulse from the lithotripter propagated at a speed of 1.5 mm μs^{-1} and had a spatial extent of approximately 10 mm. Therefore the pulse remained in a region of the order of 100 mm around the focal region for a time of order 100 μs. Pressures were measured in the focal region with a fibreoptic laser hydrophone for various voltage setting of the lithotripter. At 8 kV, the positive peak pressure is 10 MPa and the lateral width (full width at half maximum (FWHM), −6 dB) is 10 mm. The acoustic energy in the focal plane that passes through a circle of 12 mm diameter is 8 mJ. At 12 kV, the positive peak pressure is 49 MPa and the lateral width (FWHM, −6 dB) is only 4 mm with an acoustic energy in the focal plane that passes through a circle of 12 mm diameter of 34 mJ. At 16 kV, the positive peak pressure reaches 110 MPa. For an order of magnitude estimate of the particle velocity associated with the acoustic pulse we note that for a plane harmonic wave, $p = \rho c u_a$, where p is the pressure, ρ is the density, c is the speed of sound in the medium and u_a is the particle velocity. Taking values of $\rho = 998.2$ kg m^{-3}, $c = 1482$ m s^{-1} (distilled water at 20 °C) and a maximal pressure of 110 MPa this yields a particle velocity of about 74 m s^{-1}.

It should be noted that the velocity measurements presented in the following section were taken either prior to the pulse reaching the measurement region (and therefore prior to any particle velocity propagating in this region) or at times between 1 and 40 ms after the pulse had propagated through the focal region. In the latter case the pulse will have passed the measurement region and will have been mainly absorbed (figure 1). Therefore no particle velocities associated with the acoustic pulse were measured as this was not the focus of the research. The residual pressures (due to diffraction and partial reflection) at the times of measurement were in the range 1 –10 bar and therefore the errors associated with optical refraction were considered to be negligible. In the following sections the results of visualizations and velocity measurements for an acoustic lens with a focus at $x = 80$ mm $y = 0$ mm are presented.

3.1. Bubble visualizations

Visualizations of the bubble cluster at a discharge voltage of 16 kV are shown in figure 3 in terms of a series of images in which the time separation between the images, δt, varies between 40 and 700 μs. In all pairs of images the first image of the pair was obtained at the same time corresponding to the discernible formation of a stable bubble cluster. This time was found by a process of trial and error. The bubble cluster captured at this point of time varied in terms of the position of the individual bubbles, however, the extent of the bubble cluster, the number of bubbles and the average size of the bubbles were consistent in all cases. The images were taken with the seeding particles added to the water to ensure that the characteristics of the bubble cluster depicted in figure 3 correspond to the bubbles cluster generated during the PIV measurements. A number of visualizations were performed prior to adding the seeding particles and the bubble cluster was found to be qualitatively similar to that formed after the seeding. This suggests that the nylon particles did not change the phenomenon that was already occurring with the tap water. The centre of the focus is 10 mm from the left hand edge of the image where the bubble cluster is at its narrowest. After the focus the bubble cluster is seen to expand, this corresponds to the divergence of the lithotripter pulse. It is seen that the bubble cluster extends over the entire length of the image with a width vertically of approximately 10 mm at the focus. The bubble dynamics can be assessed by comparing the two images in each pair. The evolution of the bubbles depends on the position of the bubbles in the cluster. Bubbles at the periphery grow to a smaller size and collapse earlier than the bubbles at the centre. The following analysis of the images in figure 3 describes the bubbles in the central region for a discharge voltage of 16 kV, thus enabling a comparison between the evolution of the bubble cluster and the velocity measurements presented in section 3.2. In figure 3(a) there is a small, but noticeable increase in the size of the bubbles over the 40 μs between the images. In figure 3(b) and (c) a successively larger increase in the bubble size is evident. In figure 3(b) the radii of the bubbles are observed to increase by between 10 and 15% over 100 μs and in figure 3(c) the radii of the bubbles increase by between 15 and 25% in 400 μs. In figrues 3(d), (e) and (f), the number of bubbles remaining after 500, 600 and 700 μs respectively is reduced greatly. This indicates that, on average, the bubbles are increasing over a timescale of approximately 500 μs and then decay rapidly. The maximum diameter of the bubbles is typically between 2 and 3 mm. It is apparent from comparisons of figures 3(a)–(c) that, apart from the bubble growth, there is no discernible mean bubble motion. These bubble images provide no evidence of fluid flow prior to cavitation; this is investigated further in the following section.

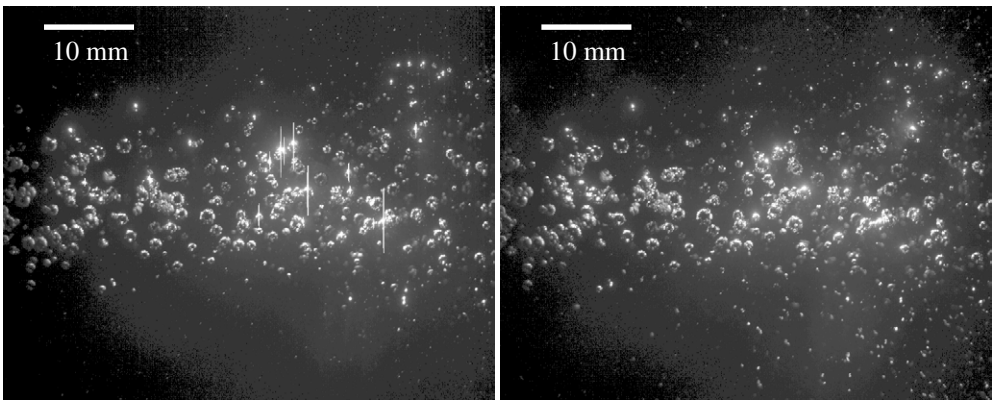

(a) $\delta t = 40\ \mu$s.

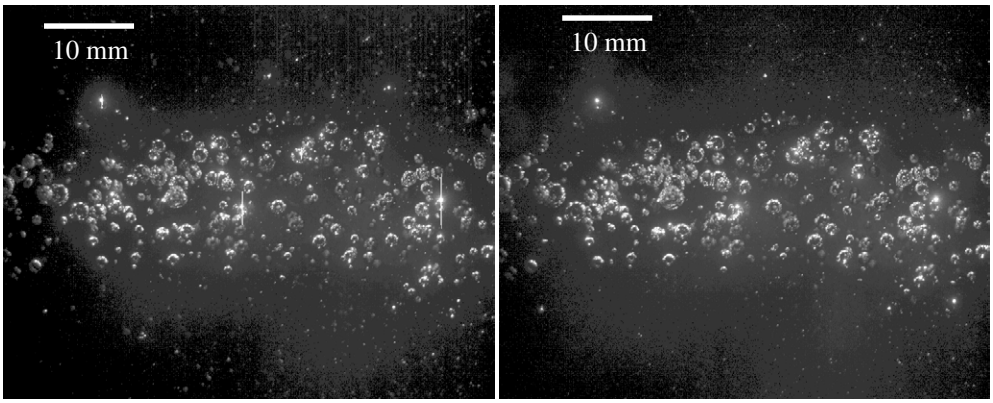

(b) $\delta t = 100\ \mu$s.

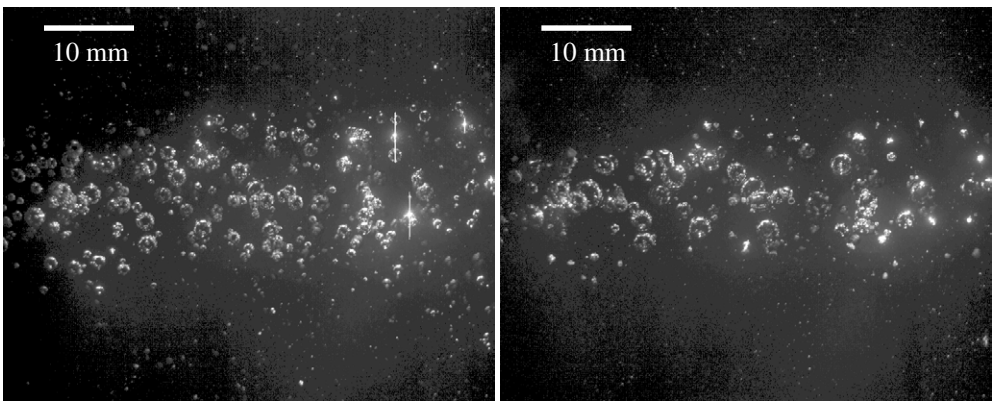

(c) $\delta t = 400\ \mu$s.

Figure 3. For caption see following page.

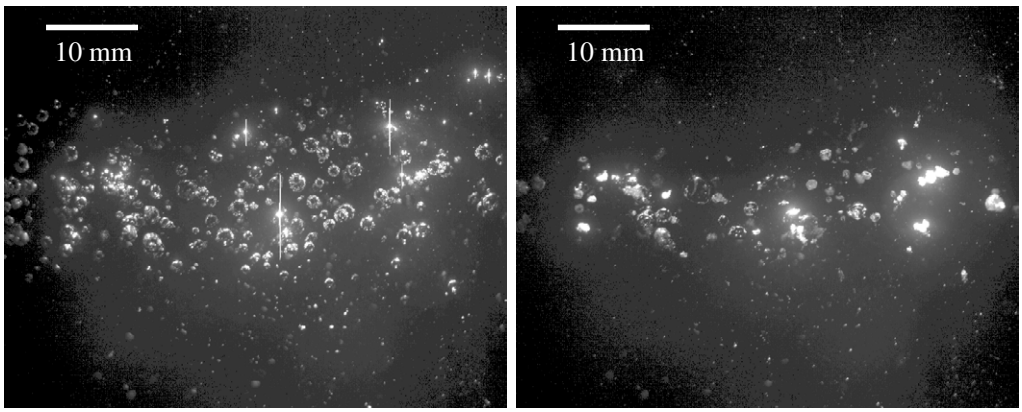

(d) $\delta t = 500\ \mu$s.

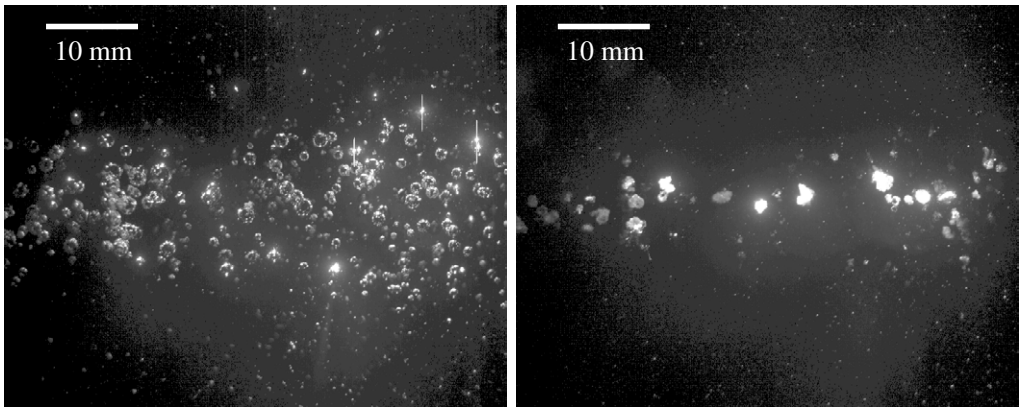

(e) $\delta t = 600\ \mu$s.

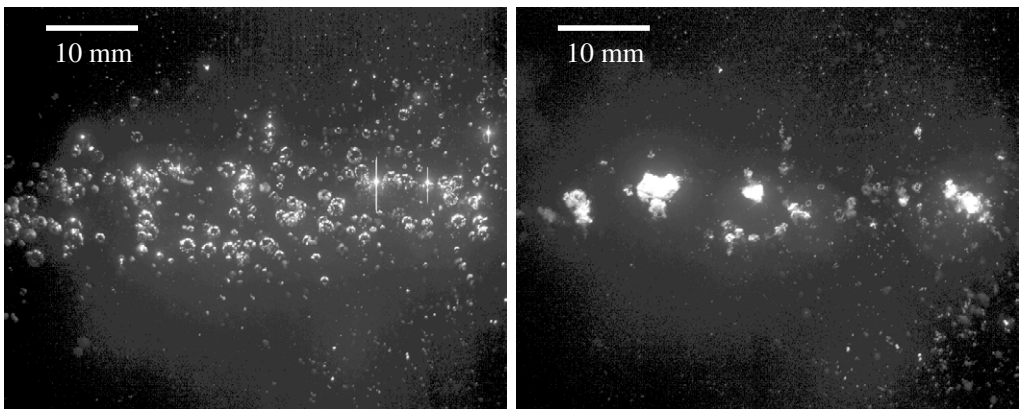

(f) $\delta t = 700\ \mu$s.

Figure 3. Image pairs with varying separations δt for a discharge voltage of 16 kV.

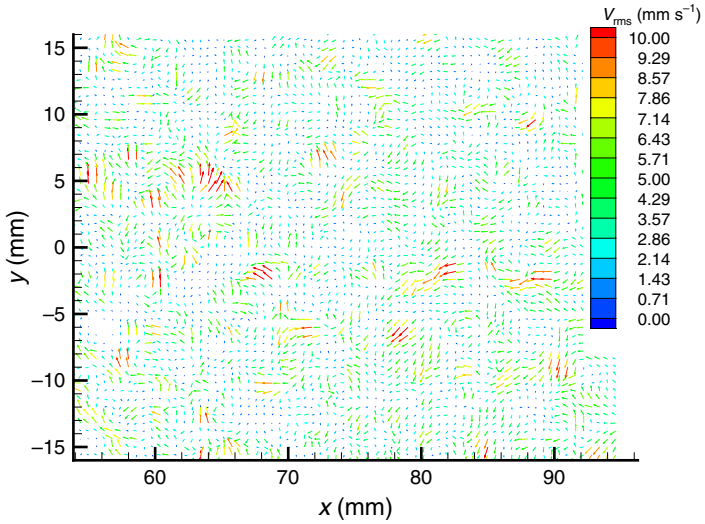

Figure 4. Instantaneous velocity field taken just prior to the formation of the bubble cluster for a discharge voltage of 16 kV.

3.2. Velocity and shear fields

The previous subsection indicated that the cavitation was random in terms of the location of individual bubbles from discharge to discharge of the lithotripter. As is shown in the following results, the velocity field formation varied when taken under the same experimental conditions of pulse intensity and spatial and temporal location. Instantaneous measurements give details of the velocity field at a specific time and are useful for determining quantities such as the maximum flow velocity or shear rate and determining where these values occur relative to, for example, a collapsing bubble. However, due to the random nature of the bubble cluster, it is necessary to consider average results to obtain details of the general characteristics of the flow. The results are presented in terms of the measured velocity fields and also the shear rate, γ. In two-dimensions the shear rate is given by

$$\gamma = \frac{\partial u}{\partial y} + \frac{\partial v}{\partial x}, \tag{1}$$

where u and v are the velocities in the x- and y-directions, respectively; however, for calculation purposes this is approximated by the finite difference

$$\gamma(i, j) = \frac{u_{i,j+1} - u_{i,j-1}}{y_{i,j+1} - y_{i,j-1}} + \frac{v_{i+1,j} - v_{i-1,j}}{x_{i+1,j} - x_{i-1,j}}, \tag{2}$$

where i and j are integer indices corresponding to the x- and y-coordinates, respectively.

To observe whether streaming occurred prior to cavitation a large number of velocity maps were recorded. Figure 4 shows one such instantaneous velocity field captured just at the onset of cavitation (in the second image small cavitation bubbles can be observed) for a discharge voltage of 16 kV. The vector map indicates that the velocities are generally much less than 10 mm s^{-1}. The velocities that are of the order 10 mm s^{-1} generally occur in regions where a small bubble is

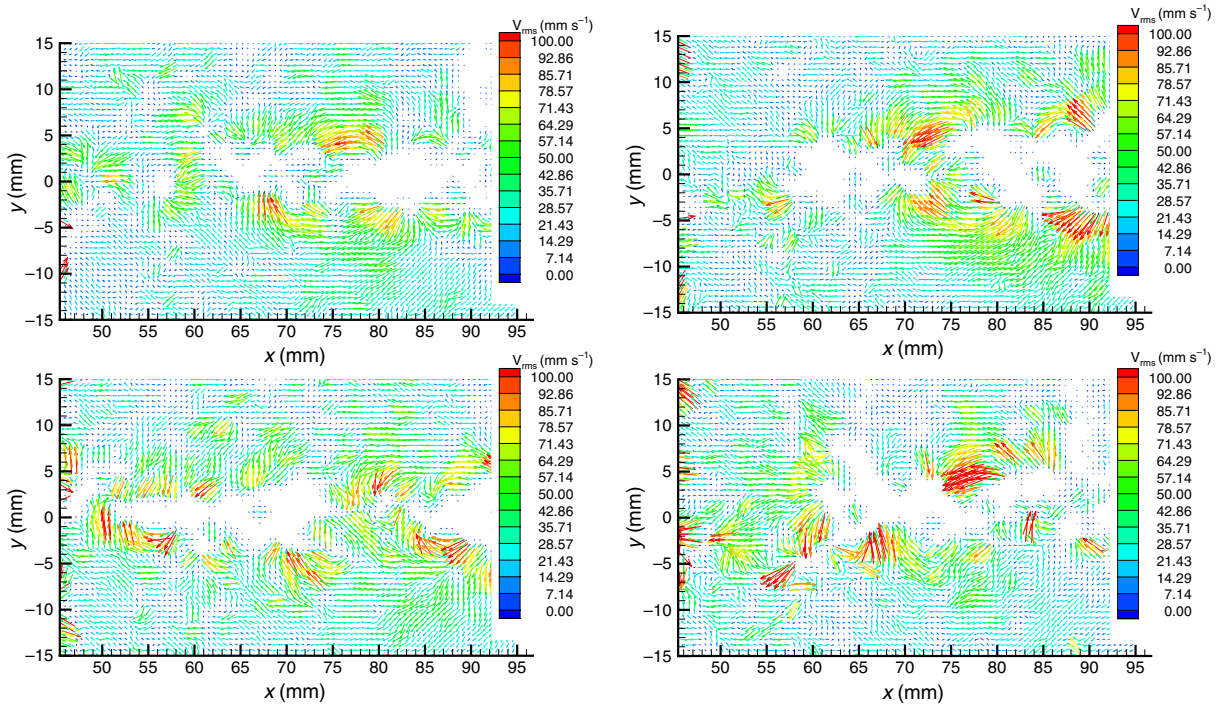

Figure 5. Instantaneous velocity field 1 ms after the pressure pulse passes the focal region for four different discharges of 16 kV.

observed in the second image of a pair and therefore are due to the expanding bubble interacting with the fluid medium. Generally the velocities are of order 1 mm s^{-1} which is the order of the settled fluid motion between experiments. This map is typical of those recorded prior to cavitation.

The velocity vector fields given in figure 5 show four separate measurements which were taken 1 ms after the pressure pulse had passed the focus for a discharge voltage of 16 kV. In each case the measurement region is between $x = 45$ and 95 mm from the acoustic lens and the focus is at $x = 80$ mm, $y = 0$ mm. In each velocity map the flow can be seen to consist of a number of small localized circulations, the largest of which is generally close to the focus. There are also a number of regions where no velocities have been measured; these correspond to regions in the fluid where a number of miniature collapsed bubbles appear on the images and the correlation procedure is not able to calculate the fluid velocity. For each measurement in figure 5 the velocities of the circulations are typically between 50 and 100 mm s^{-1}. The local nature of the circulations suggests that the flow had developed from the growth and collapse of the bubbles, rather than from streaming generated by the pressure pulse. This is further suggested by the absence of any significant velocity prior to cavitation. Figure 6 shows the corresponding shear rate for the flows in figure 5. The velocity vectors have been included also in figure 6 to indicate how the regions of high shear relate to the local circulations. The rate of shear, γ, is seen to take values of up to $\pm 50\,s^{-1}$. The shear rate is calculated from the gradient of the velocity, so a high shear rate is obtained from the relatively slow flow due to its local nature.

Figure 7(a) shows the velocity field 1 ms after the pressure pulse passed the focus for a discharge voltage of 12.7 kV. The flow pattern is similar to that observed for a discharge voltage

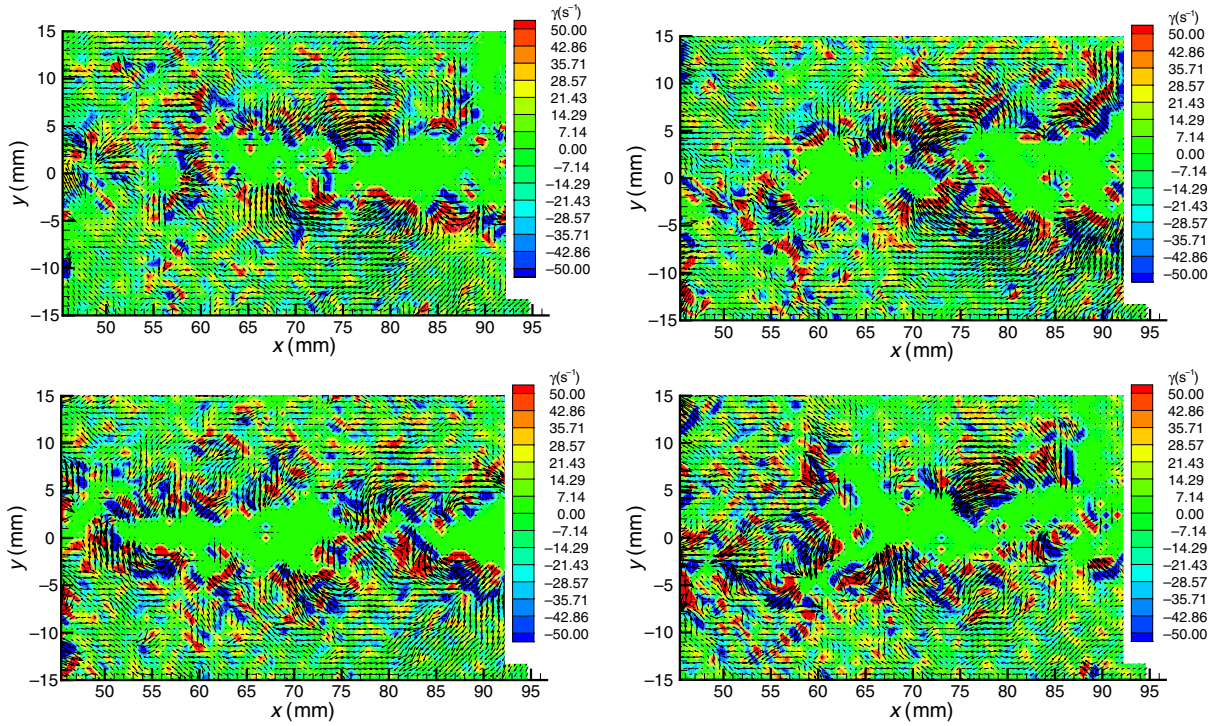

Figure 6. Instantaneous shear rate 1 ms after the pressure pulse passes the focal region for four different discharges of 16 kV.

of 16 kV, see figure 5. In particular, the flow pattern is again made up of a number of small localized circulations corresponding to local bubble events. The magnitude of the velocities is, however, significantly smaller; the maximum measured velocity is of the order of 25 mm s^{-1}. The corresponding shear rate, γ, is shown in figure 7(b). As would be expected it shows similar features to figure 6, that is localized regions of high shear rate, with a maximum shear rate of $\gamma \simeq \pm 10\ s^{-1}$.

To obtain a full picture of the general trends of the fluid motion it is useful to consider the average velocity. This is presented in figure 8 at 4 and 5.5 ms after the pressure pulse had passed in a region between $x = 70$ and 125 mm, for a discharge voltage of 16 kV. At both times the average is taken over 20 repeated measurements. Also a magnified view of the average velocity field is shown. The averaging procedure highlights the basic features of the flow and smooths out local events. For this reason the magnitude of the velocities obtained in the average vector maps is smaller than those observed in instantaneous images. It is clear from figure 8 that between 4 and 5.5 ms after the pressure pulse had passed, the fluid motion was still dominated by local circulations derived from the cavitation bubbles. Figure 9 shows the averaged velocity and shear rate results at 40 ms after the pressure pulse had passed. Evidence of the initial circulations was still present. However, a mean flow had developed in the positive x-direction with a magnitude of 10–20 mm s^{-1}. This flow was observed at tens of milliseconds after the pressure pulse had passed. In figure 9(a) there are a number of circulations to be seen at the edge of the mean flow and there are also flow variations within the mean flow region. These variations were responsible for the areas of shear which can be observed in figure 9(b).

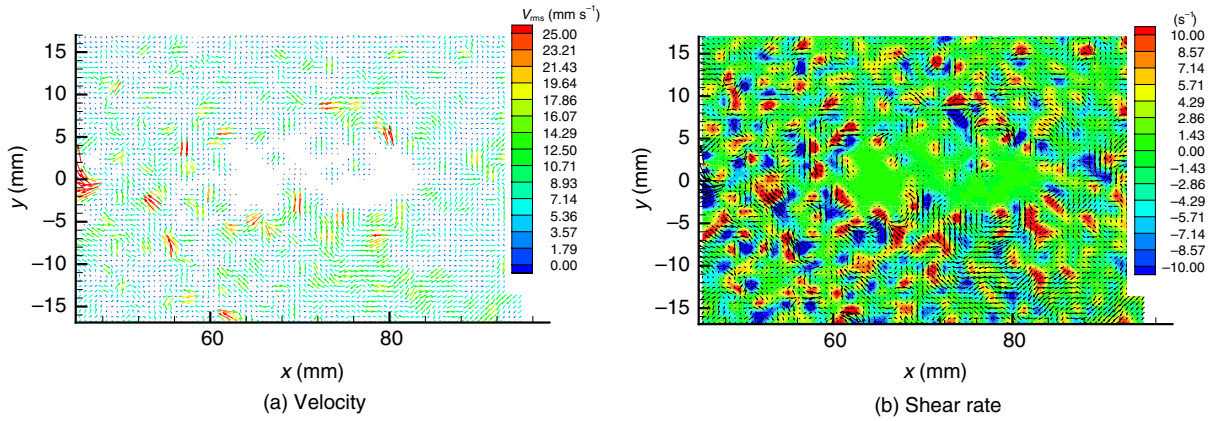

Figure 7. Instantaneous (a) velocity and (b) shear rate 1 ms after the pressure pulse passed the focal region for a discharge voltage of 12.7 kV.

The instantaneous flows observed several milliseconds after cavitation had measured velocities of the order of 100 mm s^{-1}. Streaming generated by nonlinear effects of the pressure pulse would occur as the pulse propagated over the area of interest. Then, following the initial impulse from the pressure wave the flow would be momentum driven. However, no clearly discernible streaming velocities were observed just prior to cavitation which is where a streaming jet would be maximal. Furthermore, no net motion of the bubbles in the cavitation region were observed. Finally, the velocities after cavitation had occurred were of the same order as those of the circulations set-up by the collapsing bubbles. Therefore, it is concluded that the mean flow observed was due to the collapsing bubbles and that there was no acoustic streaming seen in the timescale or length-scale of the measurements. As the flow moved out from the position in which it was generated, a number of local motions merged to produce a larger flow structure. This process was repeated until a large-scale flow pattern developed. The uni-directional nature of the flow observed 40 ms after the pulse has passed the focal region was a consequence of the lack of rotational symmetry in the original bubble cluster.

Arora *et al* [12] have considered the dynamics of the bubble cluster produced by a two layer piezoelectric transducer with a charging voltage of 5 kV. The fluid velocity in a 21.4 × 21.4 mm^2 area about the focus was also considered in terms of the variation in the magnitude of the maximum velocity with time and a map of the velocity field 150 ms after bubble collapse. Due to the differences in the lithotripters and the power settings a direct quantitative comparison is not possible; however, it is interesting to qualitatively compare the results. The instantaneous velocity field presented by Arora *et al* (figure 10(b) in [12]) 150 ms after the collapse of the bubble cluster is quantitatively similar to the velocity field presented here, in the same region (70 mm $< x <$ 90 mm), in figures 5 (instantaneous), 8(c), (d) (averaged) and 9(b) (averaged) at times 1, 4, 5.5 and 40 ms, respectively. That is, both sets of measurements show local circulations derived from the cavitation bubbles. Arora *et al* did not consider the region where a mean flow is observed in figure 9. As well as these qualitative similarities, we also note that there is a considerable difference in terms of timescale. Arora *et al* reports a maximum velocity in the focal region approximately 200 ms after bubble collapse.

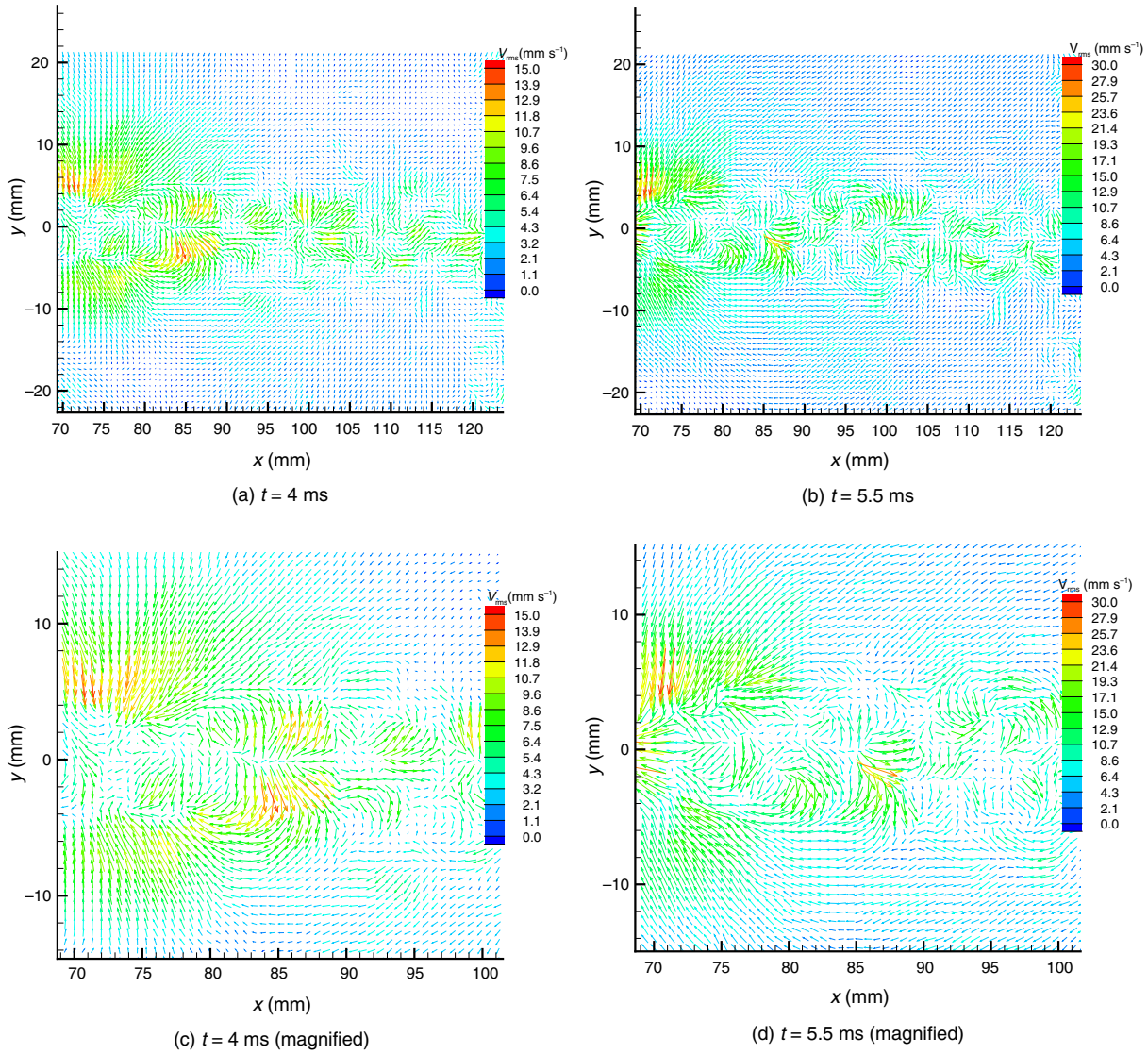

Figure 8. Averaged velocity field (a) 4 ms and (b) 5.5 ms after the pressure pulse from lithotripter passed the focal region. Magnified views are shown in (c) and (d). The discharge voltage was 16 kV.

4. Conclusions and future work

Visualizations of the bubble cluster and quantitative velocity measurements in the focal region of a lithotripter have been performed. The average lifetime of the bubbles was of the order of 500 μs during which they were seen to grow to a maximum size of 2–3 mm before suddenly collapsing. PIV measurements were taken in the region of the lens focus prior to, during and after cavitation. No discernible streaming motion was observed in the time interval between the pressure pulse reaching the focus and the start of cavitation. During and shortly after cavitation the velocity field consisted of a number of localized flows which were associated with the growth and collapse of cavitation bubbles. At time intervals of the order of milliseconds after cavitation the maximum velocities observed were of the order of 100 mm s^{-1} with associated shear rates

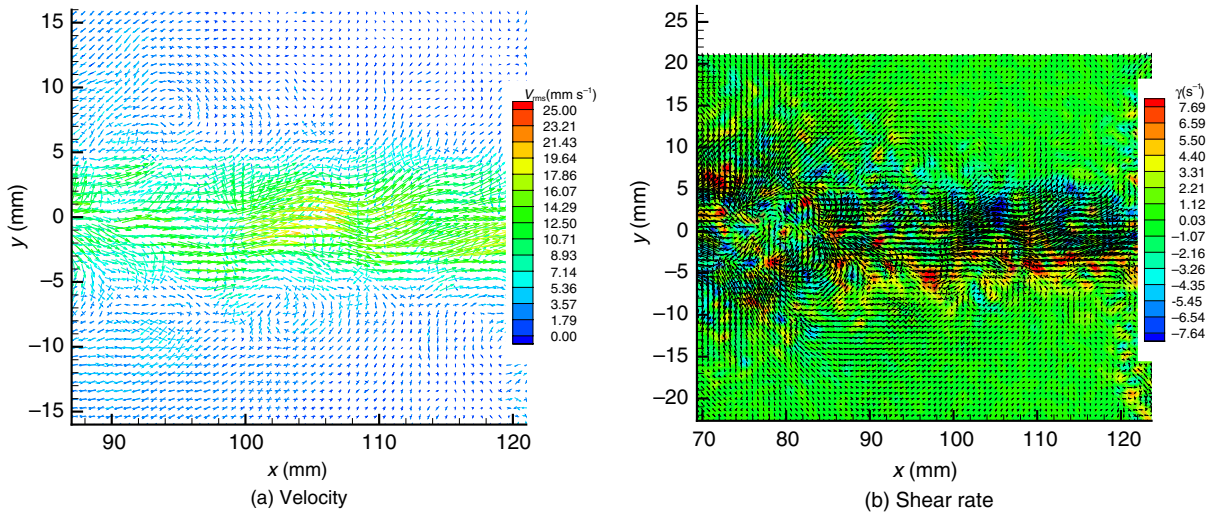

Figure 9. Averaged (a) velocity and (b) shear rate field 40 ms after the pressure pulse from lithotripter passed the focal region.

of the order of 50 s^{-1}. Average velocity fields with a mean flow in the positive x-direction (the direction of propagation of the pulse) were observed 40 ms after the pulse had passed. It is concluded that this flow was derived from the localized flow fields associated with the bubble cluster rather than an acoustic streaming jet. During cavitation, velocities of the order of 1 ms^{-1} were observed, however, refraction effects close to the bubble cluster rendered normal PIV error estimates redundant and therefore this can be considered only a qualitative estimate. Further work is required to establish the extent to which image capture and subsequent PIV analysis is altered due to variations in the refractive index of the fluid as the pressure pulse passes. The effect of refractive index change can be seen in the images of [24] where the pressure pulse was visualized using a Schlieren technique, although there is no quantitative estimate of how this distorts the images. It is of interest also to investigate the interaction between the cavitation bubbles and a surface. This is the situation which occurs when the lithotripter is applied to kidney stone removal. In such circumstances it is possible that the overall flow field would be dominated by high velocity jets arising from asymmetrical bubble collapse.

Acknowledgments

We would like to acknowledge the support of Dornier MedTech.

Appendix. Radiation force on the seeding particles

For the motion of the seeding particles to match that of the surrounding fluid it is essential that any additional forces acting on the particles are negligible. The seeding particles had a relative density of 1.03 and so gravity can be neglected. The particles also experienced a radiation force as the pulse passed. Following [15] the influence of the radiation force can be considered. The radiation force on a spherical particle of relative

density Λ and radius a in a fluid of density ρ, when subject to a plane progressive wave described by a velocity potential of magnitude A is [25]

$$F = 2\pi\rho A^2 (ka)^6 \frac{[1 + 2(1 - \Lambda)^2/9]}{(2 + \Lambda)^2}, \tag{A.1}$$

where k is the wavenumber for the wave. Here we are considering a pulse, rather than a progressive wave; however an estimation of the radiation force can be obtained where $k = 2\pi/L$, where L is the spacial extend of the pulse and $A = P/\rho\omega$, where P is the maximum recorded pressure and $\omega = ck$. With $P = 110$ MPa and $L = 10$ mm, this gives a radiation force of $F = 5.6 \times 10^{-13}$ N. Finally, equating this force to the drag on a sphere gives a terminal velocity (due to the radiation force)

$$v_\infty = \frac{F}{6\pi\,\mu a}, \tag{A.2}$$

where μ is the viscosity of the fluid. That is the terminal velocity that a particle would reach if the radiation force was applied continuously. Here $v_\infty = 2.9 \times 10^{-3}$ mm s^{-1}. This is negligible relative to the measured velocities.

References

[1] Chaussy C H, Brendel W and Schmiedt E 1980 Extracorporeally induced destruction of kidney stones by shock waves *Lancet* **316** 1265–8

[2] Brennen C E 1995 *Cavitation and Bubble Dynamics* (Oxford: Oxford University Press)

[3] Holmer N G, Almquist L O, Hertz T G, Holm A, Lindstedt E, Persson H W and Hertz C H 1991 On the mechanism of kidney stone disintegration by acoustic shock waves *Ultrasound Med. Biol.* **17** 479–89

[4] Coleman A J, Choi M J and Saunders J E 1996 Detection of acoustic emission from cavitation in tissue during extracorporeal lithotripsy *Ultrasound Med. Biol.* **22** 1079–87

[5] Evan A P, Willis L R, McAteer J A, Bailey M R, Connors B A, Shao Y, Lingeman J E, Williams J C Jr, Fineberg N S and Crum L A 2002 Kidney damage and renal functional changes are minimized by waveform control that suppresses cavitation in shock wave lithotripsy *J. Urol.* **168** 1556–62

[6] Church C C 1989 A theoretical study of cavitation generated by an extracorporeal shock wave lithotripter *J. Acoust. Soc. Am.* **86** 215–27

[7] Sapozhnikov O A, Khokhlova V A, Bailey M R, Williams J C Jr, McAteer J A, Cleveland R O and Crum L A 2002 Effect of overpressure and pulse repetition frequency on cavitation in shock wave lithotripsy *J. Acoust. Soc. Am.* **112** 1183–95

[8] Katz J I 1999 Jets from collapsing bubbles *Proc. R. Soc.* A **455** 323–8

[9] Jöchle K, Debus J, Lorenz W J and Huber P 1996 A new method of quantitative cavitation assessment in the field of a lithotripter *Ultrasound Med. Biol.* **22** 329–38

[10] Zhong P, Cioanta I, Cocks F H and Preminger G M 1997 Internal cavitation and associated acoustic emission produced during electrohydraulic shock wave lithotripsy *J. Acoust. Soc. Am.* **101** 2940–50

[11] Zhong P, Lin H, Xi X, Zhu S and Bhogte E S 1999 Shock wave-inertial microbubble interaction: Methodology, physical characterization and bioeffect study *J. Acoust. Soc. Am.* **105** 1997–2009

[12] Arora M, Junge L and Ohl C D 2005 Cavitation cluster dynamics in shock-wave lithotripsy: Part 1. Free field *Ultrasound Med. Biol.* **31** 827–39

[13] Sokolov D L, Bailey M R and Crum L A 2001 Use of a dual-pulse lithotripter to generate a localized and intensified cavitation field *J. Acoust. Soc. Am.* **110** 1685–95

[14] Lokhandwalla M, McAteer J A, Williams J C Jr and Sturtevant B 2001 Mechanical haemolysis in shock wave lithotripsy (SWL): II. In vitro cell lysis due to shear *Phys. Med. Biol.* **46** 1245–64
[15] Cosgrove J A, Buick J M, Campbell D M and Greated C A 2001 PIV applied to acoustical phenomena *Proc. 8th Int. Congress on Sound and Vibration* ed L Cheng, K M Li and R M C So (Hong-Kong: China) pp 479–86
[16] Goldstein R J 1996 *Fluid Mechanics Measurements* (London: Taylor and Francis) chapter 4
[17] Raffel M, Wilert C and Kompenhans J 1998 *Particle Image Velocimetry — A Practical Guide* (Berlin: Springer)
[18] Westerweel J 1993 *Digital particle image velocimetry—theory and applications PhD Thesis* Delft University, The Netherlands
[19] Blake J R and Gibson D C 1987 Cavitation bubbles near boundaries *Annu. Rev. Fluid Mech.* **19** 99–123
[20] Campbell M, Cosgrove J A, Greated C A, Jack S and Rockliff D 2000 Review of LDA and PIV applied to the measurement of sound and acoustic streaming *Opt. Laser Technol.* **32** 629–39
[21] Cosgrove J A, Buick J M, Pye S D and Greated C A 2001 PIV applied to Eckart streaming produced by a medical ultrasound transducer *Ultrasonics* **39** 461–4
[22] Nyborg W L 1965 *Acoustic Streaming in Physical Acoustics* vol II (part B) (NewYork: Academic) chapter 11
[23] Schlichting H 1968 *Boundary-Layer Theory* (New York: McGraw-Hill)
[24] Ohl C D 2002 Cavitation inception following shock wave passage *Phys. Fluids* **14** 3512–21
[25] King L V 1934 On the acoustic radiation pressure on spheres *Proc. R. Soc. Lond.* A **147** 212–40